



Non-Rare-Earth $\text{Na}_3\text{AlF}_6:\text{Cr}^{3+}$ Phosphors for Far-Red Light-Emitting Diodes

Dechao Yu,*[†] Yuanshu Zhou,[†] Chenshuo Ma,[†] Jonathan H. Melman,[‡] Kristen M. Baroudi,[‡] Mikio LaCapra,[†] and Richard E. Riman*,[†]

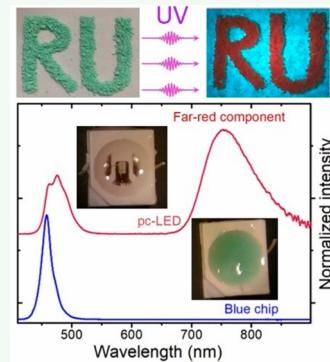
[†]Department of Materials Science and Engineering, Rutgers, The State University of New Jersey, 607 Taylor Road, Piscataway, New Jersey 08854, United States

[‡]Lumenari, Inc., 1501 Bull Lea Road, Suite 105, Lexington, Kentucky 40511, United States

Supporting Information

ABSTRACT: Emerging phototherapy in a clinic and plant photomorphogenesis call for efficient red/far-red light resources to target and/or actuate the interaction of light and living organisms. Rare-earth-doped phosphors are generally promising candidates for efficient light-emitting diodes but still bear lower quantum yield for the far-red components, potential supply risks, and high-cost issues. Thus, the design and preparation of efficient non-rare-earth activated phosphors becomes extremely important and arouses great interest. Fabrication of Cr^{3+} -doped Na_3AlF_6 phosphors significantly promotes the potential applications by efficiently converting blue excitation light of a commercial InGaN chip to far-red broadband emission in the 640–850 nm region. The action response of phototherapy (~667–683 nm; ~750–772 nm) and that of photomorphogenesis (~700–760 nm) are well overlapped. Based on the temperature-dependent steady luminescence and time-resolved spectroscopies, energy transfer models are rationally established by means of the configurational coordinate diagram of Cr^{3+} ions. An optimal sample of $\text{Na}_3\text{AlF}_6:60\%$ Cr^{3+} phosphor generates a notable QY of $75 \pm 5\%$. Additionally, an InGaN LED device encapsulated by using $\text{Na}_3\text{AlF}_6:60\%$ Cr^{3+} phosphor was fabricated. The current exploration will pave a promising way to engineer non-rare-earth activated optoelectronic devices for all kinds of photobiological applications.

KEYWORDS: fluorescence, non-rare-earth, Cr^{3+} , far-red, LEDs



INTRODUCTION

Plant cultivation in horticulture, as well as phototherapy to treat physical illness, has been significantly stimulated by the emergence of efficient red and far-red light-emitting diodes (LEDs).^{1,2} For plant growth, photosynthesis requires red light radiation in the 600–690 nm range to overlap well with the respective absorption peaks of chlorophylls *a* and *b* at 662 and 642 nm.^{2,3} Particularly, plant morphogenesis encompasses the light-mediated seed germination, seedling development, and photoperiodism, which is critical to healthy plant development. On the other hand, for phototherapy, there exist several active response bands located in the red and far-red light regions: (i) 613–623 nm, (ii) 667–683 nm, and (iii) 750–772 nm.^{4,5} A growing body of evidence indicates photoacceptors in cells, like cytochrome *c* oxidase and the terminal enzyme of mitochondrial electron transport chain, exhibit response to low-intensity red light and even near-infrared light.⁶ Exposure to 670 or 726 nm LEDs red light was reported to decrease the healing time in chronic ischemic ulcers in rats.^{7,8} Therefore, achievement of novel red/far-red sources would significantly promote the development of plant cultivation and phototherapy.

Phosphor-converted light-emitting diodes (pc-LEDs) have been emerging as indispensable solid state light sources

because of their unique merits such as energy savings, environment-friendliness, small footprint, long operational lifetime, and so on.⁹ However, the deficiency of far-red light components limits LEDs applications in natural light sources, plant cultivation, phototherapy, and so on.¹⁰ Typically, rare-earth (RE) ions like Eu^{3+} , Eu^{2+} , Pr^{3+} , and Sm^{3+} are doped as activators into numerous hosts for red/far-red emissions under ultraviolet (UV) or blue excitation,¹¹ but the wide applications are limited by the following features: (i) Eu^{3+} , Pr^{3+} , and Sm^{3+} ions feature intra-4f parity-forbidden electronic transitions which have relatively weak absorption and therefore a low external quantum yield (QY);^{12–14} (ii) Eu^{2+} has an allowed $4f^7 \rightarrow 4f^65d^1$ transition with about 1000 times larger absorption than the intra-4f parity-forbidden transitions, but nearly all Eu^{2+} -doped red/far-red phosphors exhibit a relatively low external QY $\leq 70\%.$ ^{11,15,16} Besides, RE elements have additional issues due to potential supply risk and high cost, and hence non-RE activated phosphors become extremely important and currently arouse great interest.^{17–19} Moreover, the recent commercial success of potassium fluorosilicate-

Received: August 18, 2019

Accepted: October 6, 2019

Published: October 7, 2019

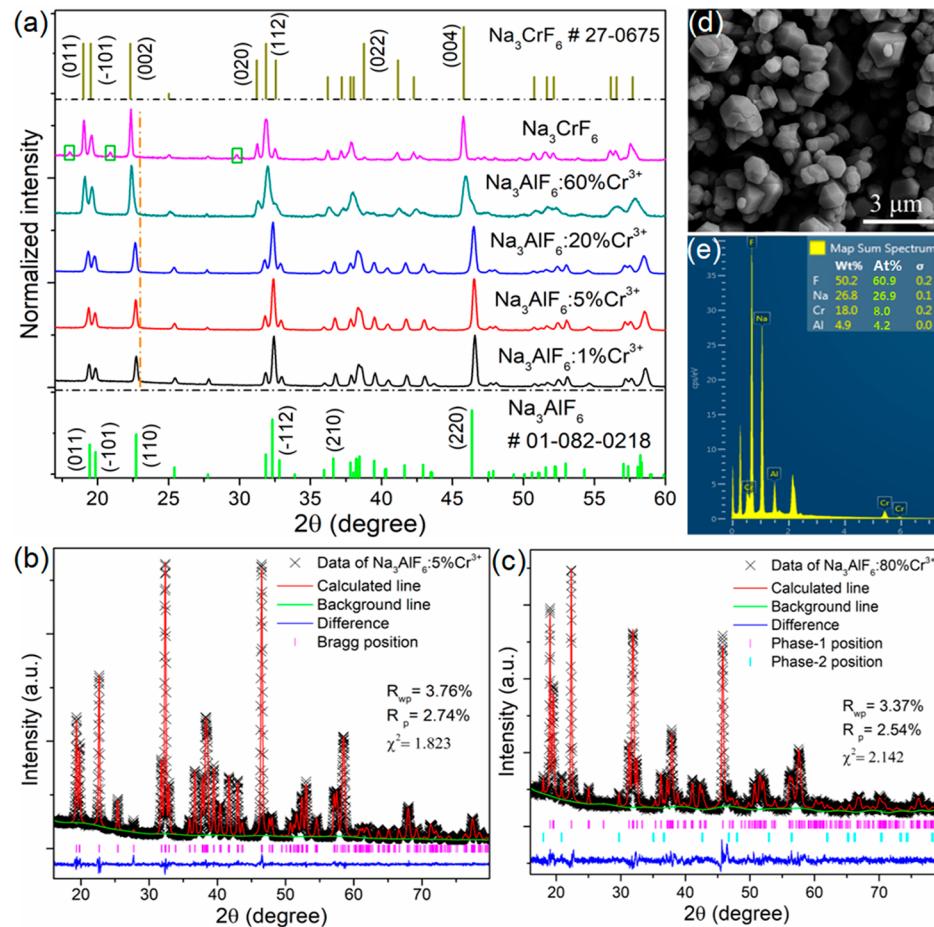


Figure 1. (a) XRD patterns of $\text{Na}_3\text{AlF}_6\text{:}x\%$ Cr^{3+} ($x = 1, 5, 20, 60, 100$) representatives and that of Na_3AlF_6 (PDF #01-082-0218) and Na_3CrF_6 (PDF #27-0675) standards. The green frames label the coexisting byproducts, $(\text{NH}_4)_2\text{NaCrF}_6$, as the Cr^{3+} doping concentration exceeds 60–70% (see detailed discussion in Figures S1 and S2). (b, c) XRD Rietveld refinement results for the samples of 5% Cr^{3+} (b) and 80% Cr^{3+} (c) doped Na_3AlF_6 showing raw data (black crosses) and calculated (red solid line) XRD profiles, difference between the raw data and calculated patterns (blue solid line), and Bragg reflection positions (pink and neon blue short vertical lines). (d) SEM micrographs and (e) EDX spectra analysis of the as-prepared $\text{Na}_3\text{AlF}_6\text{:}60\%$ Cr^{3+} sample.

based phosphors ($\text{K}_2\text{SiF}_6\text{:Mn}^{4+}$) in LED applications has spurred new interest in the properties of non-oxide materials.^{20,21} The manganese(IV) system has shown that peak emission wavelengths can be broadly modified when moving from an oxide system to a fluoride system.¹⁹

The Cr^{3+} ion has been well studied since the first generation of working lasers, i.e., the ruby ($\alpha\text{-Al}_2\text{O}_3\text{:Cr}^{3+}$) laser's coherent far-red light at 694.3 nm.²² Absorption bands of Cr^{3+} originate from interconfiguration spin-allowed transitions of ${}^4\text{A}_2 \rightarrow {}^4\text{T}_2$ (4F), ${}^4\text{A}_2 \rightarrow {}^4\text{T}_1$ (4F), and ${}^4\text{A}_2 \rightarrow {}^4\text{T}_1$ (4P). Their oscillator strengths are typically on the order of 10^{-4} ,²³ which is at least hundreds of times more than that of the representative intra-4f transitions of RE ions, such as Eu^{3+} : ${}^7\text{F}_0 \rightarrow {}^5\text{D}_0$ about 1.3×10^{-8} ,²⁴ Pr^{3+} : ${}^3\text{H}_4 \rightarrow {}^1\text{D}_2$ about $(0.3\text{--}1.5) \times 10^{-6}$,¹⁴ and Sm^{3+} : ${}^6\text{H}_{5/2} \rightarrow {}^6\text{P}_{3/2}, {}^4\text{F}_{7/2}$ about 9.3×10^{-6} .²⁵ Therefore, Cr^{3+} -activated materials feature a significantly larger absorption cross-section, especially the ${}^4\text{A}_2 \rightarrow {}^4\text{T}_1$ (4F) blue absorption on the order of 10^{-18} cm^2 ,²⁶ about 1000-fold greater than that of the RE ions on the order of 10^{-21} cm^2 .²⁷ Additionally, in the case of low crystal field surrounding Cr^{3+} , the site emitting will occur from the ${}^4\text{T}_2$ (4F) level to the ${}^4\text{A}_2$ ground level, which is a spin-allowed transition.²⁸ Manipulation of the environment surrounding Cr^{3+} can tailor the emission peak of ${}^4\text{T}_2$ (4F) \rightarrow ${}^4\text{A}_2$ in the 650–1600 nm range.²⁹ Also, the ${}^4\text{T}_2$ (4F) \rightarrow ${}^4\text{A}_2$

transition of Cr^{3+} is typically about 2 orders of magnitude stronger than the ${}^2\text{E} \rightarrow {}^4\text{A}_2$ parity-forbidden transition of Cr^{3+} occurring in high crystal field.³⁰ Accordingly, these optical advantages of Cr^{3+} significantly enable the fabrication of efficient, advanced red/far-red emitting phosphors for blue-light-excited LEDs for photobiology.

In the current work, we synthesized a series of polycrystalline $\text{Na}_3\text{AlF}_6\text{:}x\%$ Cr^{3+} ($x = 0\text{--}100$) phosphors by means of a facile hydrothermal reaction. A broad ${}^4\text{T}_2$ (4F) \rightarrow ${}^4\text{A}_2$ emission band spanning 640–850 nm can be efficiently generated under excitation of UV/blue/orange light. Moreover, emission peak of ${}^4\text{T}_2$ (4F) \rightarrow ${}^4\text{A}_2$ was obtained with a continuous red-shifting from 710 to 745 nm as Cr^{3+} concentration increases to $x \sim 100$. It is of great interest that the intensity of ${}^4\text{T}_2$ (4F) \rightarrow ${}^4\text{A}_2$ monotonically increase until higher Cr^{3+} concentration $x \sim 60$ with a maximum QY of $75 \pm 5\%$. Energy transfer dynamics of Cr^{3+} ions and the capabilities of photobiological application were systematically analyzed by means of time-resolved spectra and by an encapsulated blue light InGaN LED device, respectively.

EXPERIMENTAL SECTION

Hydrothermal Synthesis of $\text{Na}_3\text{AlF}_6\text{:}x\%$ Cr^{3+} Particles.

Utilizing NH_4F ($\geq 98\%$), NaF ($\geq 98\%$), $\text{Al}(\text{NO}_3)_3 \cdot 9\text{H}_2\text{O}$ ($\geq 98\%$),

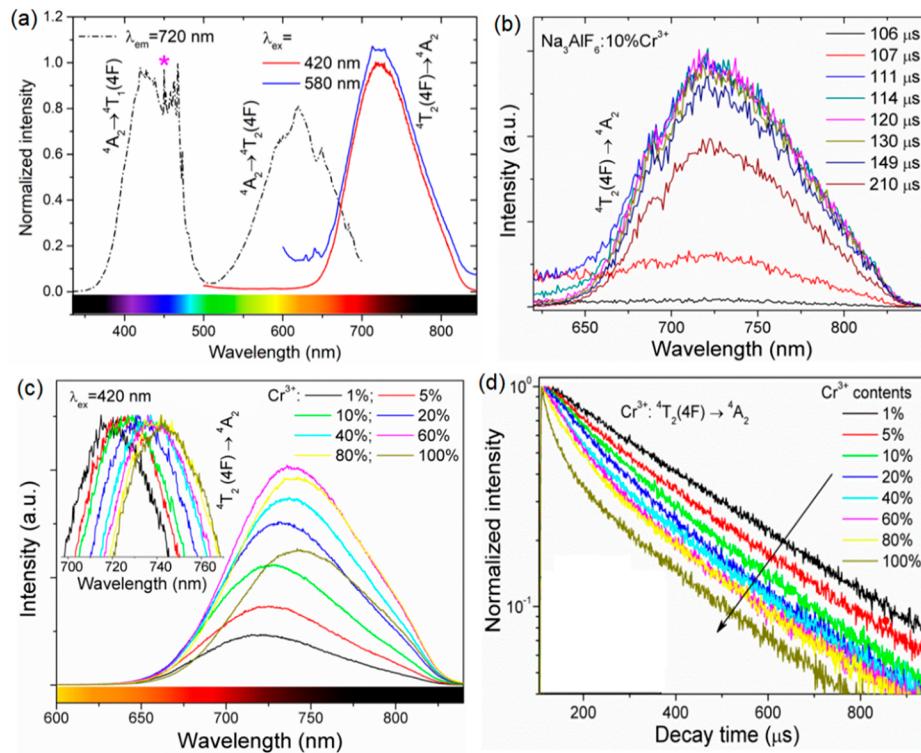


Figure 2. (a) Excitation ($\lambda_{\text{em}}: 720 \text{ nm}$) and emission ($\lambda_{\text{ex}}: 420$ and 580 nm) spectra of $\text{Na}_3\text{AlF}_6:1\%$ Cr^{3+} phosphors. The pink star labels the sharp interference light peaks typically from Xe lamp around 467 nm. (b) Time-resolved emission spectra of $\text{Na}_3\text{AlF}_6:10\%$ Cr^{3+} under pulsed light excitation of 420 nm. (c) Emission spectra and (d) decay curves of $\text{Na}_3\text{AlF}_6:x\%$ Cr^{3+} ($x = 1, 5, 10, 20, 40, 60, 80, 100$) phosphors. The inset of (c) shows the normalized emission peaks of $\text{Na}_3\text{AlF}_6:x\%$ Cr^{3+} phosphors.

and $\text{Cr}(\text{NO}_3)_3 \cdot 9\text{H}_2\text{O}$ (99%) as raw materials (all purchased from Sigma-Aldrich), we synthesized a series of $\text{Na}_3\text{AlF}_6:x\%$ Cr^{3+} ($x = 0.5, 1, 5, 10, 20, 30, 40, 50, 60, 70, 80, 90, 100$) phosphors by a hydrothermal reaction. In all cases, the percentages given for Cr^{3+} dopant is in mol % with respect to the Al^{3+} site. First, the specified stoichiometric $\text{Al}(\text{NO}_3)_3 \cdot 9\text{H}_2\text{O}$ and $\text{Cr}(\text{NO}_3)_3 \cdot 9\text{H}_2\text{O}$ were weighed and then dissolved by 30 mL of deionized (DI) water (18.2 MΩ) under magnetic stirring in a glass beaker. Second, excess NaF and NH_4F with >9 times molar ratio to metal ions (Al^{3+} and/or Cr^{3+}) were measured and added into another 30 mL of DI water for dissolution. Third, the NaF and NH_4F solution was transferred into the above $\text{Al}(\text{NO}_3)_3$ and $\text{Cr}(\text{NO}_3)_3$ solution for reaction, and then 10 mL of absolute ethanol was added additionally. At last, after vigorous stirring for about 30 min, the resultant white suspension was transferred into a 125 mL Teflon-lined stainless-steel autoclave (Parr Instrument Company), filled up to 70% of its capacity, sealed tightly, and heated at 240 °C in an electrical furnace for 15 h. After being slowly cooled to room temperature, the filtered precipitate was centrifuged several times with DI water to remove any possible ionic remnant and finally dried at 80 °C for 24 h in an ambient atmosphere.

Post-Heat Treatment of $\text{Na}_3\text{AlF}_6:60\%$ Cr^{3+} Powder. The as-obtained $\text{Na}_3\text{AlF}_6:60\%$ Cr^{3+} phosphor was pressed into a quarter inch diameter pellet by using a hydraulic press and then placed in a quartz ampule which was sealed under vacuum for post-heat treatment. The ampule was inserted into a furnace and heated from room temperature to 700 °C for 2.5 h, dwelled at 700 °C for 36 h, and cooled to room temperature over 2.5 h. After heating, the ampule was opened in the air and the pellet was removed. The pellet was ground in an agate mortar and pestle for several minutes to produce a powder. The powder was stored with a desiccant after grinding.

Characterization. Phase identification of all the as-obtained phosphor samples were performed on a Siemens D500 X-ray powder diffractometer (XRD, Bruker AXS Inc., Madison, WI) using $\text{Cu K}\alpha$ ($\lambda = 1.5406 \text{ \AA}$) radiation at 40 kV and 40 mA. XRD patterns were collected with a resolution of $0.018^\circ/\text{step}$ and $2 \text{ s}/\text{step}$ in a 2θ range

of 10° – 60° . Scanning electron microscopy (SEM) images of the respective powder samples were taken by means of the Carl Zeiss Sigma field emission SEM (Carl Zeiss, Carl Zeiss SMT Inc., Peabody, MA) using the secondary electron detector and operating at an accelerating voltage of 5.0 kV with a working distance of 8.8 mm. Energy-dispersive X-ray (EDX) spectroscopy area scans of the $\text{Na}_3\text{AlF}_6: x\%$ Cr^{3+} powder samples were further performed to determine the elemental composition using an accelerated voltage of 15 kV and a reduced working distance of 8.5 mm for an aperture of $60 \mu\text{m}$.

Steady photoluminescence and excitation spectra were determined via single photon counting technique on a FSP920 spectrometer (Edinburgh Instruments, Livingston, UK) equipped with a 450 W xenon (Xe) lamp, TMS300 monochromators, and thermo-electronic cooled Hamamatsu R928P photomultiplier tube (PMT) detector. Time-resolved spectra were measured by time-correlated single photon counting technique on the FSP920 system with pulsed excitation sources of a microsecond μF900 Xe lamp. To eliminate signal noise from excitation sources, long-pass filters of 400, 490, 695, and 710 nm were appropriately applied in the front of detectors. Temperature-dependent fluorescence spectra of $\text{Na}_3\text{AlF}_6: 60\%$ Cr^{3+} were measured by using a Fluorolog-3 spectrophotometer (Horiba Jobin Yvon) equipped with a FL-1073 PMT detector and a SPEX DM302 P.C. Acq. module. The phosphors were heated on an external hot plate, and each temperature point was allowed to equilibrate as monitored by a thermocouple in a sand bath adjacent to the phosphors. Once the temperature was equilibrated, the emission spectrum of the hot sample was measured ($\lambda_{\text{ex}} = 450 \text{ nm}$) and compared to a room temperature sample of the phosphor to eliminate the impact of lamp intensity fluctuations. For comparison, all optical measurements were rigorously performed under identical conditions for each series of testing.

Fluorescence QY of phosphors was measured on a C9220-03 system (Hamamatsu, Bridgewater, NJ) with a 150 W Xe monochromatic lamp and an integrating sphere. A high-intensity

365 nm UV lamp (B-100A, UVP, LLC, CA) was used to shine phosphors for optical photographs. LEDs devices were fabricated by applying a 25 wt % phosphor slurry composed of the phosphor powder and Dow Corning OE-6550 silicone on top of a blue-emitting InGaN based LED mounted in a 2835 PLCC package (Power Opto Co., Taiwan), followed by thermal curing of the LEDs package on a hot plate at 125 °C.

RESULTS AND DISCUSSION

As shown in Figure 1a and Figure S1, all the XRD profiles of as-obtained $\text{Na}_3\text{AlF}_6:x\%$ Cr³⁺ ($x = 0.5, 1, 5, 10, 20, 40, 60, 80, 100$) powders can be indexed as peaks corresponding to pure cryolites of Na_3AlF_6 with PDF card no. 01-082-0218 (also ICSD card no. 74202) and Na_3CrF_6 (PDF card no. 27-0675). When the Cr³⁺ concentration exceeds 60–70%, a secondary phase emerges with observed XRD patterns around 17°, 20.8°, and 29.7° (see the frame labels in Figure 1a and Figure S1). By completely going through XRD database, the impurities can be well indexed into the phase of $(\text{NH}_4)_2\text{NaAlF}_6$ (PDF #97-024-9157; Figures S1 and S2a). Crystalline Na_3AlF_6 and Na_3CrF_6 both have structures with space group of $P2_1/n$ and space group number of 14 (monoclinic Na_3AlF_6 for ICSD #74202: $a = 5.454 \text{ \AA}$, $b = 5.616 \text{ \AA}$, $c = 7.822 \text{ \AA}$, $\alpha = \gamma = 90^\circ$, and $\beta = 90.118^\circ$; orthorhombic Na_3CrF_6 : $a = 5.460 \text{ \AA}$, $b = 5.680 \text{ \AA}$, $c = 7.880 \text{ \AA}$, and $\alpha = \beta = \gamma = 90^\circ$). Powder XRD pattern Rietveld refinement for $\text{Na}_3\text{AlF}_6:5\%$ Cr³⁺ and $\text{Na}_3\text{AlF}_6:80\%$ Cr³⁺ was further performed to gain more structural information (Figures 1b and 1c). The main parameters of processing and refinement of the $\text{Na}_3\text{AlF}_6:x\%$ Cr³⁺ ($x = 5, 80$) samples are listed in Table S1. The refinement results in Figure 1b reveal that the as-obtained $\text{Na}_3\text{AlF}_6:5\%$ Cr³⁺ sample is all pure monoclinic Na_3AlF_6 (pink short vertical line in Figure 1b), and the weighted *R*-factor (R_{wp}) and profile *R*-factor (R_p) are determined to be 3.76% and 2.74%, respectively, indicating that the refined results are reliable. Whereas for $\text{Na}_3\text{AlF}_6:80\%$ Cr³⁺, the Rietveld refinements from XRD patterns of Na_3CrF_6 phase (pink short vertical line in Figure 1c) and $(\text{NH}_4)_2\text{NaAlF}_6$ phase (neon blue vertical lines in Figure 1c) further confirm that the concentrated Cr³⁺ doping, such as more than 60–70%, does introduce a secondary phase of byproducts, $(\text{NH}_4)_2\text{NaAlF}_6$ and/or $(\text{NH}_4)_2\text{NaCrF}_6$. Through calculation, there generally exists more than 3% impurities in the $\text{Na}_3\text{AlF}_6:80\%$ Cr³⁺ phosphors, which will not influence the following studies on the optical properties of $\text{Na}_3\text{AlF}_6:\text{Cr}^{3+}$ phosphors (see fluorescence comparison in Figure S2b and Figure 2).

Given that the effective ionic radius of Al³⁺ [$r = 0.535 \text{ \AA}$, coordination number (CN) = 6] is considerably close to that of Cr³⁺ ($r = 0.615 \text{ \AA}$, CN = 6)³¹ and that no charge compensation needed during substitution, Na_3AlF_6 is a perfect host to continuously vary Cr³⁺ concentration from a regime where it acts as a dopant to a regime where it likely serves as a constituent. As a direct proof of the solid solution, increasing substitution of Al³⁺ (smaller radius) by Cr³⁺ (larger radius) from 1% to 100%, the XRD peaks like (002) profile of the as-prepared phosphors smoothly shift toward smaller angle relative to the peaks of pure Na_3AlF_6 and finally match well with that of pure Na_3CrF_6 (Figure 1a and Figure S1). This phenomenon verifies the incorporation of Cr into the lattice. Furthermore, the lattice parameters (a , b , c , and V) refined from the measured XRD patterns feature increasing behaviors with increasing x (Figure S3), which, well consistent with Vegard's rule,³² demonstrate the $\text{Na}_3\text{AlF}_6:x\%$ Cr³⁺ ($x = 0.5–$

100) solid solutions are formed by us. Within the monoclinic “mixed-cation fluoride perovskite” structure of Na_3AlF_6 cryolite crystals, the corner-sharing octahedral network comprises alternating $[\text{AlF}_6]^{3-}$ and $[\text{NaF}_6]^{5-}$ octahedra with Na⁺ ions in interstitial sites (Figure S4).³³ The low symmetry of the $[\text{AlF}_6]^{3-}$ octahedral site in this structure that would be further disordered by Cr³⁺ doping (Figure S4) is expected to benefit the spin-allowed transitions of Cr³⁺, especially the $^4\text{T}_2(4\text{F}) \rightarrow ^4\text{A}_2$ red/far-red emission in a low crystal field.³⁴

From the SEM micrograph of Na_3AlF_6 : 60% Cr³⁺ representative in Figure 1d, it can be seen that the prepared phosphors are well crystallized into polyhedron and have size distribution from 250 nm to 1.25 μm . To explore elemental composition as well as its distribution of Cr³⁺-doped Na_3AlF_6 phosphors, EDX mapping analysis was done for the $\text{Na}_3\text{AlF}_6:60\%$ Cr³⁺ sample (Figure 1e and Figure S5). The EDX elemental composition was determined by comparing relative peak intensities together with the corresponding sensitivity factors of each element and assuming their total intensities to be 100%. All the elements of Na⁺, Al³⁺, F⁻, and Cr³⁺ were clearly detected (Figure 1e) and homogeneously mapped in the as-obtained phosphors (Figure S5). EDX results reveal the mole percent of Cr³⁺ and that of Al³⁺ are further calculated to be about 66% and 34%, respectively, which are very close to the stoichiometric compositions of 60% Cr³⁺ and 40% Al³⁺ in the prepared sample.

To investigate the photoluminescence properties of $\text{Na}_3\text{AlF}_6:\text{Cr}^{3+}$ phosphors, excitation and emission spectra were recorded for the $\text{Na}_3\text{AlF}_6:1\%$ Cr³⁺ representative, shown in Figure 2a. By monitoring the emission wavelength at 720 nm, we detected two excitation peaks (420 and 620 nm) due to the d-d inner transitions of Cr³⁺ from the $^4\text{A}_2$ ground state to the $^4\text{T}_1(4\text{F})$ and $^4\text{T}_2(4\text{F})$ intermediate states,^{35–37} respectively. By increasing Cr³⁺ concentration, the excitation peaks were observed to perform noticeable red-shift after normalizing all the excitation spectra at wavelength $\sim 420 \text{ nm}$ (Figure S6a). Under excitation of 282, 420, and 580 nm, the $\text{Na}_3\text{AlF}_6:1\%$ Cr³⁺ phosphors yield one single broad peak at about 720 nm (Figure 2a and Figure S6b) due to the spin-allowed transition of $^4\text{T}_2(4\text{F}) \rightarrow ^4\text{A}_2$ in the case of Cr³⁺ located in the low crystal field.²⁸ The color rendering index of $\text{Na}_3\text{AlF}_6:x\%$ Cr³⁺ phosphors was calculated to be around (0.723, 0.276) and displayed by CIE chromaticity coordinates in Figure S7. Taking into account the crystal field strength and site symmetry of Na_3AlF_6 host, the underlying mechanisms of photoexcitation and energy transfer of Cr³⁺ activators were discussed and illustrated by a simplified Tanabe–Sugano diagram of 3d³ electron configuration in Figure S8. It is noted that the broadband emission of $\text{Na}_3\text{AlF}_6:\text{Cr}^{3+}$ generally spans from 640 to 850 nm, has a full width at half-maximum of about 95 nm, and overlaps well with the “active” peaks at about 670, 760, and 825 nm of cells and DNA/RNA synthesis for phototherapy.^{5,6}

To explore whether or not any different Cr³⁺ luminescent centers exist in $\text{Na}_3\text{AlF}_6:x\%$ Cr³⁺, time-resolved emission spectra with a fine time interval of 0.5 μs were recorded for the sample of $\text{Na}_3\text{AlF}_6:10\%$ Cr³⁺ under pulsed light excitation of 420 nm (Figure 2b). At initial delay time around 106 μs , no emission band appears, while a single broad band centered at about 720 nm emerges clearly at delay time around 107 μs due to the energy depopulation of excited Cr³⁺ ions. By prolonging delay time, the intensity of the whole Cr³⁺ characteristic band monotonically increases to a maximum at about 120 μs and

then decreases. Notably, the band shapes and peak position of all the emissions remain unchanged at different delay time points. These results suggest that all the Cr³⁺ activators do have similar surrounding environments.

To optimize the Na₃AlF₆:x% Cr³⁺, a series of emission spectra were recorded under excitation of 420 nm, as shown in Figure 2c. The emission intensity of ⁴T₂(4F) → ⁴A₂ increases to a maximum until an elevated concentration of 60% Cr³⁺ and then decreases obviously because of the concentration quenching effect. Such an effect mainly results from the energy consumption via energy migration over Cr³⁺ sublattice sites and finally to the quenching sites, like impurities/defects particularly as the higher Cr³⁺ concentration in Na₃AlF₆ makes the Cr³⁺-to-Cr³⁺ interatomic distance much smaller.^{38,39} In comparison with the emission intensity of Na₃AlF₆:1% Cr³⁺, that of Na₃AlF₆:60% Cr³⁺ exhibits about 5-fold enhancement. The QY value was measured to be 75 ± 5% under excitation of 420 nm, which is comparable to the QY value ~68% reported by Torchia et al.⁴⁰ It is of great interest that the normalized emission peaks in the inset of Figure 2c show the distinct red-shift from 715 to 745 nm, which would benefit the color component manipulation according to the varied specific applications like in phototherapy and/or photomorphogenesis. The red-shift results from the perturbation effects of crystal field strength on the ⁴T₂(4F) spin-allowed state of Cr³⁺ with increasing Cr³⁺ concentration in Na₃AlF₆. Generally, the crystal field strength (D_q) can be formulized as^{41,42}

$$D_q = \frac{1}{6} Z e^2 \frac{r^4}{R^5} \quad (1)$$

where Z is the anion charge or valence, e is the electron charge, r is the radius of the d wave function, and R is the bond length. So the dependence of D_q on bond length can be generalized as $D_q \propto 1/R^5$ in a specific host. Doping Cr³⁺ ions (radius ~0.615 Å) into Na₃AlF₆ by substituting Al³⁺ sites (radius ~0.535 Å) will lead to a longer R of the Cr–F bond and therefore a weaker D_q crystal strength. Correspondingly, a smaller D_q leads to emission at lower energy, namely, the resultant red-shift at higher Cr³⁺ concentration. Experimentally, the obvious red-shift of absorption peaks of Na₃AlF₆:Cr³⁺ phosphors (Figure S6) well demonstrate such an effect of weaker D_q on lowering the energy of ⁴T₂(4F) spin-allowed state of Cr³⁺. Besides, by greatly increasing Cr³⁺ concentration, the severe reabsorption occurring in the 650–710 nm range (see the overlapping range between absorption and emission in Figure 2a) would be another promotion to this red-shift for the photoluminescence of Na₃AlF₆:Cr³⁺ phosphors.

To give insight into energy-transfer process of Na₃AlF₆:x% Cr³⁺ ($x = 1, 5, 10, 20, 40, 60, 80, 100$) phosphors, the decay curve of ⁴T₂(4F) → ⁴A₂ was recorded versus Cr³⁺ concentration upon 420 nm pulsed light excitation. As shown in Figure 2d, the decay curve of dilute 1% Cr³⁺ doping behaves single exponential (similar behaviors in Figure S9 for the 0.5% Cr³⁺ and 2% Cr³⁺ doping), and that of concentrated x % Cr³⁺ doping ($x \sim 5\text{--}100$) has a faster decline and becomes obviously nonexponential. These phenomena are typically caused by the introduction of additional energy decay paths as Cr³⁺-doping concentration increases, like cross-relaxation, energy migration, and the impurity/defect-induced nonradiative relaxation (NR) process, especially for the concentrated dopants.⁹ In practice, the monoexponential decay curve can be well fitted to a first-order exponential function of $I = A_0 \exp(-t/\tau_0)$, and the nonexponential one is well fitted to a

second-order exponential function of $I = A_1 \exp(-t/\tau_1) + A_2 \exp(-t/\tau_2)$, where I is the luminescence intensity; A_0 , A_1 , and A_2 are constants of fitting parameters, respectively; t is time; τ_0 is the lifetime for the monoexponential decay curve; and τ_1 and τ_2 are fast and slow lifetime of exponential components for the nonexponential decay curve, respectively. Using the formula $\tau = (A_1\tau_1^2 + A_2\tau_2^2)/(A_1\tau_1 + A_2\tau_2)$, we can obtain the average decay time (τ) of the second-order exponential decay for the Na₃AlF₆:x% Cr³⁺ samples. The t_{rise} , fitting function, R -squared (R^2), fitting parameters, and τ are summarized as a function of Cr³⁺ concentration in Table 1.

Table 1. Fitting Functions, R-Squared (R^2), Fitting Parameters, and the Calculated Decay Time of Decay Curve of ⁴T₂(4F) → ⁴A₂ Luminescence as a Function of Cr³⁺ Concentration in Na₃AlF₆ under Pulsed Light Excitation of 420 nm

Cr ³⁺ (%)	fitting function	R^2	component lifetime (μs)	fitting parameter	decay time (μs)
1	$I = A_0 \exp(-t/\tau_0)$	0.9992		$A_0 \sim 1.4826$	312.9
5	$I = A_1 \exp(-t/\tau_1) + A_2 \exp(-t/\tau_2)$	0.9993	$\tau_1 = 116.7$	$A_1 \sim 0.8176$	283.3
			$\tau_2 = 329.6$	$A_2 \sim 1.0421$	
10	$I = A_1 \exp(-t/\tau_1) + A_2 \exp(-t/\tau_2)$	0.9993	$\tau_1 = 136.1$	$A_1 \sim 1.1364$	257.5
			$\tau_2 = 333.1$	$A_2 \sim 0.7446$	
20	$I = A_1 \exp(-t/\tau_1) + A_2 \exp(-t/\tau_2)$	0.9992	$\tau_1 = 127.2$	$A_1 \sim 1.4922$	240.6
			$\tau_2 = 349.2$	$A_2 \sim 0.5678$	
40	$I = A_1 \exp(-t/\tau_1) + A_2 \exp(-t/\tau_2)$	0.9992	$\tau_1 = 79.5$	$A_1 \sim 2.0832$	219.7
			$\tau_2 = 320.8$	$A_2 \sim 0.7158$	
60	$I = A_1 \exp(-t/\tau_1) + A_2 \exp(-t/\tau_2)$	0.9991	$\tau_1 = 87.7$	$A_1 \sim 2.1914$	213.7
			$\tau_2 = 342.8$	$A_2 \sim 0.5477$	
80	$I = A_1 \exp(-t/\tau_1) + A_2 \exp(-t/\tau_2)$	0.9992	$\tau_1 = 65.7$	$A_1 \sim 2.7234$	194.4
			$\tau_2 = 304.7$	$A_2 \sim 0.6856$	
100	$I = A_1 \exp(-t/\tau_1) + A_2 \exp(-t/\tau_2)$	0.9985	$\tau_1 = 30.1$	$A_1 \sim 19.6474$	85.2
			$\tau_2 = 267.9$	$A_2 \sim 0.6666$	

To further optimize the emission properties of Na₃AlF₆:x% Cr³⁺ phosphors, the sample of Na₃AlF₆:60% Cr³⁺ was heat-treated at 700 °C for 36 h in a quartz ampule under vacuum. Figure 3a shows that the particle size of heat-treated Na₃AlF₆:60% Cr³⁺ clearly becomes larger (up to 2–3 μm) than that before. The EDX result in Figure 3b validates the detection of all elements of Na⁺, Al³⁺, Cr³⁺, and F⁻. As expected, all elements were homogeneously distributed over the heat-treated Na₃AlF₆:60% Cr³⁺ phosphors (Figure S10). Transformation of wt % (at. %) Cr³⁺ and wt % (at. %) Al³⁺ recorded by EDX element mapping (inset of Figure 3b) to mole percent in cryolite formula results in the respective values of 57.9% and 42.1%, which are close to the stoichiometric composition of Na₃AlF₆:60% Cr³⁺. These results indicate that the heat treatment at a higher temperature ~700 °C does not change the composition of phosphors. Figure 3c comparatively shows the emission spectra of Na₃AlF₆:60% Cr³⁺ phosphors before and after heat treatment. These two spectra have same band shape in the same region, but the heat treatment process increases emission intensity by about 11%. Also, the luminescence decay of heat-treated Na₃AlF₆:60% Cr³⁺ (average $\tau \sim 263.7 \mu\text{s}$) becomes obviously slower than that of sample

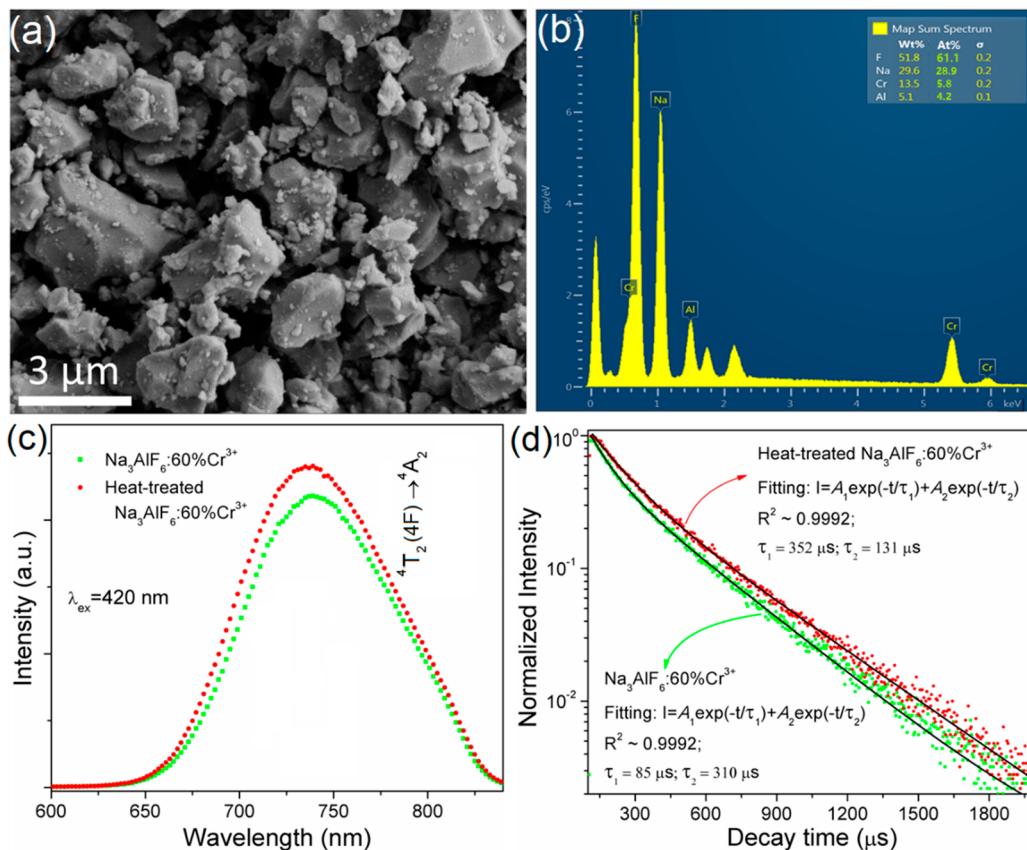


Figure 3. (a) SEM micrograph and (b) EDX spectra analysis of the $\text{Na}_3\text{AlF}_6:60\% \text{Cr}^{3+}$ phosphors heat-treated at 700°C for 36 h. (c) Comparative emission spectra and (d) decay curves of the $\text{Na}_3\text{AlF}_6:60\% \text{Cr}^{3+}$ before (green dotted curve) and after (red dotted curve) heat treatment.

without heat treatment (Table 1 and Figure 3d). This phenomenon results from the decreased amount of additional energy quenching centers, such as typical lattice/surface defects and impurities introduced by higher 60% Cr^{3+} dopants. It is believed that a continuous increase of particle size will greatly increase luminescence intensity and efficiency of our synthesized $\text{Na}_3\text{AlF}_6:\text{Cr}^{3+}$ phosphors.

For lighting phosphors, the working temperature would be much higher than room temperature. Although pc-LEDs are significantly more energy efficient light source than incandescent lighting, about 50–70% of the electricity supplied to an LED still becomes heat rather than light, and in high power packages in a more confined space, this can lead to an operating temperature of 150–200 °C during LEDs operation, which efficiently quenches photoluminescence via fast NR of excited electrons to the ground state of activators.^{43,44} Thus, study of thermal stability on the far-red emission of $\text{Na}_3\text{AlF}_6:\text{Cr}^{3+}$ phosphor is extremely important. Figure 4a shows the decay curves of the ${}^4\text{T}_2(4\text{F}) \rightarrow {}^4\text{A}_2$ for $\text{Na}_3\text{AlF}_6:60\% \text{Cr}^{3+}$ sample, and obviously the decay becomes much faster as temperature increases. By calculation, a shortest average lifetime was obtained to be $126.7 \mu\text{s}$ at 470 K ($\sim 200^\circ\text{C}$) (blue sphere symbols in Figure 4b), which suggests that the nonradiative decay of the $\text{Cr}^{3+}:{}^4\text{T}_2(4\text{F})$ excited state is thermally promoted at elevated temperature. Besides, Figure 4b exhibited the integrated emission intensity of ${}^4\text{T}_2(4\text{F}) \rightarrow {}^4\text{A}_2$ as a function of temperature for $\text{Na}_3\text{AlF}_6:60\% \text{Cr}^{3+}$ under excitation of 420 nm (red star symbols in Figure 4b). The far-red emission of Cr^{3+} is clearly quenched with increasing temperature and decreases to about 60% at 470 K . The reason

could be that a much higher 60% Cr^{3+} concentration in Na_3AlF_6 would feature severe energy migration among Cr^{3+} sublattice sites,^{38,39} and energy is quenched on defects/impurities.

A single configurational coordinate model of Cr^{3+} (simplified with only one ${}^4\text{T}_2(4\text{F})$ excited state) in Figure 4c describes the effects of thermal quenching on the far-red emission of Cr^{3+} qualitatively. Once Cr^{3+} is excited from the ${}^4\text{A}_2$ ground state to the ${}^4\text{T}_2(4\text{F})$ state, energy will go through a fast NR process to populate the lowest energy point of the ${}^4\text{T}_2(4\text{F})$. Basically, the energy in ${}^4\text{T}_2(4\text{F})$ excited state radiatively decays to the ${}^4\text{A}_2$ ground state by efficiently yielding far-red photons at room/lower temperature. However, in the case of an elevated temperature, the absorbed energy in ${}^4\text{T}_2(4\text{F})$ excited state is feasibly promoted to the intersystem crossing (Q) of ${}^4\text{T}_2(4\text{F})$ excited state and ${}^4\text{A}_2$ ground state by thermal activation (T-activation) and then is quenched by fast nonradiative decay to the bottom of ${}^4\text{A}_2$ ground state. Typically, the temperature-dependent fluorescence intensity can be expressed as^{27,28}

$$I = \frac{I_0}{1 + \beta e^{-\Delta E_q/kT}} \quad (2)$$

where I_0 is initial fluorescence intensity recorded at ideal case with negligible thermal quenching, ΔE_q is the thermal activation barrier to the level crossing Q, k is the Boltzmann constant, T is the absolute temperature, and the unit $e^{-\Delta E_q/kT}$ therefore represents the probability of an excited ion being elevated over ΔE_q barrier to the Q crossing. Accordingly, a higher temperature will thermally promote more excited ions

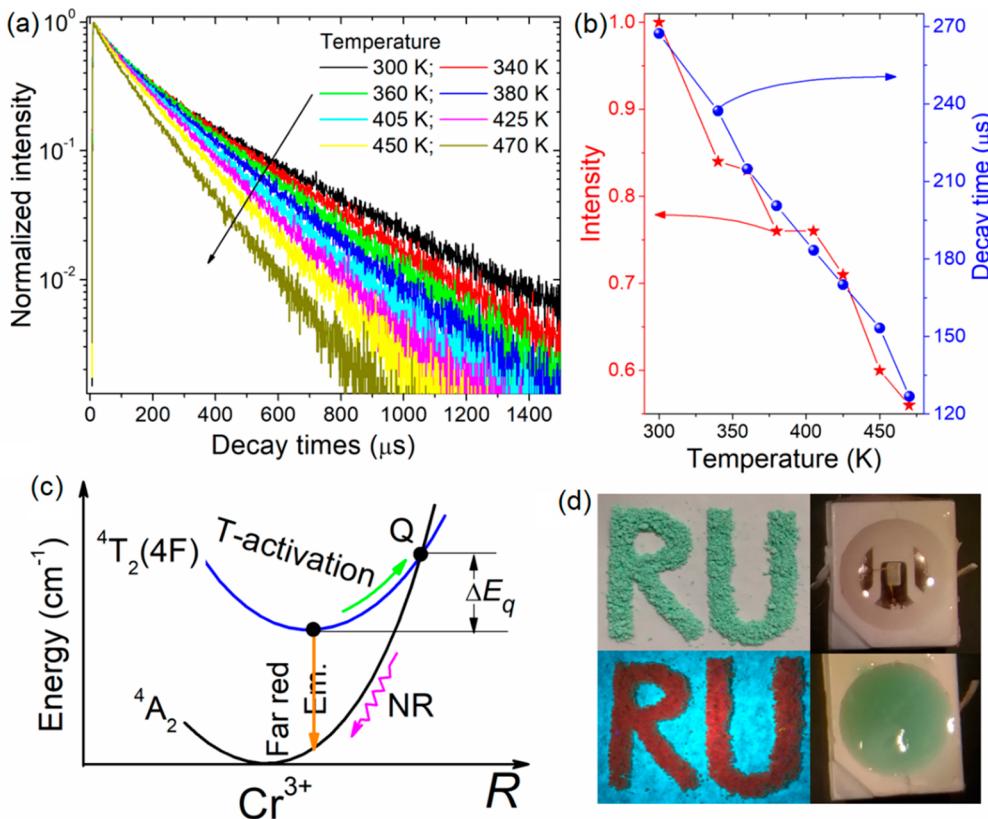


Figure 4. (a) Decay curves of ${}^4T_2(4F) \rightarrow {}^4A_2$ of Na_3AlF_6 :60% Cr^{3+} phosphors against temperature. (b) Thermal characteristics of ${}^4T_2(4F) \rightarrow {}^4A_2$ of Na_3AlF_6 :60% Cr^{3+} : emission intensity marked by red stars and the corresponding lifetime by blue spheres. (c) Single configurational coordinate model for Cr^{3+} far-red emission under effect of temperature increment in Na_3AlF_6 low-field crystal. R denotes the configurational coordinate, the green arrow indicates the thermal activation process, and the pink curved arrow represents the NR process. (d) Optical images of Na_3AlF_6 :60% Cr^{3+} phosphors shined by natural white light (left top) and UV light (left bottom) and that of a bare blue-emitting InGaN LED device (right top) and the InGaN LED device encapsulated with a silicone Na_3AlF_6 :60% Cr^{3+} phosphor slurry (right bottom).

to easily reach the level crossing Q_q and meanwhile, the stronger NR process happens. On the assumption that the photon absorption and scattering of luminescent sample keep constant in the temperature region,²⁸ fluorescence intensity of the phosphors will definitely decrease with increasing temperature under the same excitation conditions. These theoretical analyses well reveal why our Na_3AlF_6 :60% Cr^{3+} phosphor exhibits descending emission intensity by raising temperature from 300 to 470 K.

Figure 4d shows optical photographs of Na_3AlF_6 :60% Cr^{3+} phosphors illuminated by natural white light (top panel) and UV lamp (bottom panel). The distinct observation of deep red color to the naked eye confirms that the Na_3AlF_6 :60% Cr^{3+} radiates efficiently. The obtained deep red color nearly features the same color effects as Color Hex Color Codes of #960000.⁴⁵ Also, optical photographs of commercial blue-emitting InGaN LED packages encapsulated in silicone without and with inclusion of Na_3AlF_6 :60% Cr^{3+} phosphor are shown in Figure 4d. The performance of four LEDs devices operated at constant current (drive voltage 2.72 V, drive current 14 mA) is shown in Figure S11. The first device is the bare blue LED; devices 1–3 are blue LEDs encapsulated with increasing amounts of Na_3AlF_6 :60% Cr^{3+} phosphors, which efficiently convert a higher percentage of the blue light to far-red light.

CONCLUSIONS

Polycrystalline Cr^{3+} -doped Na_3AlF_6 phosphors are synthesized by means of a facile hydrothermal reaction. Tunable broadband far-red fluorescence of Cr^{3+} was feasibly achieved under blue light excitation by increasing the substitution of Cr^{3+} ions into Al^{3+} sublattice sites. Na_3AlF_6 :60% Cr^{3+} phosphors exhibit an appreciable QY $\sim 75\%$ which is more efficient than some typical Eu^{2+} -doped red/far-red phosphors, and the luminescence intensity and efficiency further increased by heat treatment. ET mechanisms, as well as energy decay dynamics of Cr^{3+} , are rationally analyzed on the basis of photoemission, excitation, and time-resolved spectra. Non-RE activated red/far-red emitting phosphors in commercial LED further promote the design and fabrication of advanced p-LEDs for photobiological applications.

ASSOCIATED CONTENT

S Supporting Information

The Supporting Information is available free of charge on the ACS Publications website at DOI: 10.1021/acsaelm.9b00527.

XRD patterns of as-synthesized Na_3AlF_6 : $x\%$ Cr^{3+} phosphors (Figure S1), XRD patterns of $(\text{NH}_4)_2\text{NaAlF}_6$ and emission spectra of Na_3AlF_6 :60% Cr^{3+} and $(\text{NH}_4)_2\text{NaAlF}_6$: $x\%$ Cr^{3+} ($x = 1, 60$) phosphors (Figure S2), main parameters of processing and refinement of the Na_3AlF_6 : $x\%$ Cr^{3+} ($x = 5, 80$) samples (Table S1), calculated lattice parameters of Na_3AlF_6 : $x\%$ Cr^{3+}

samples (Figure S3), crystal structures of monoclinic Na_3AlF_6 cryolite crystal (Figure S4), EDX mapping analysis of Na_3AlF_6 :60% Cr^{3+} sample (Figure S5), emission and normalized excitation spectra for Na_3AlF_6 :x% Cr^{3+} (Figure S6), CIE chromaticity coordinates of Na_3AlF_6 :x% Cr^{3+} (Figure S7), a simplified Tanabe–Sugano diagram of $3d^3$ electron configuration (Figure S8), decay curves of Cr^{3+} : ${}^4\text{T}_1(4\text{F}) \rightarrow {}^4\text{T}_2(4\text{F})$ emission of Na_3AlF_6 :x% Cr^{3+} ($x = 0.5, 1, 2$) samples (Figure S9), EDX mapping analysis of post-heat-treated Na_3AlF_6 :60% Cr^{3+} samples (Figure S10), luminescence spectra of the bare blue-emitting InGaN LED device and three pc-LED devices with increasing phosphor loading (Figure S11) (PDF)

AUTHOR INFORMATION

Corresponding Authors

*E-mail d.yu@uu.nl.

*E-mail riman@rutgers.edu.

ORCID

Dechao Yu: [0000-0001-8132-0951](https://orcid.org/0000-0001-8132-0951)

Notes

The authors declare no competing financial interest.

ACKNOWLEDGMENTS

This work is financially supported by the National Science Foundation, National Institutes of Health, NIH NIBIB EB018378-01 (R.E.R. and D.Y.) and the Department of Energy through the Critical Materials Institute. This material is based upon work supported by the National Science Foundation under Grant # IIP-1059286 to the American Society for Engineering Education. D.Y. thanks Peixin Li and Ting Yu for the “cryolite” crystal structure analysis, Xinxin Han for the XRD Rietveld refinement, and Atul D. Sontakke for helpful discussions.

REFERENCES

- Bula, R. J.; Morrow, R. C.; Tibbitts, T. W.; Barta, D. J.; Ignatius, R. W.; Martin, T. S. Light-Emitting Diodes as A Radiation Source for Plants. *HortScience* **1991**, *26*, 203–205.
- Yeh, N.; Chung, J. P. High-brightness LEDs-Energy Efficient Lighting Sources and Their Potential in Indoor Plant Cultivation. *Renewable Sustainable Energy Rev.* **2009**, *13*, 2175–2180.
- Zabiliūtė, A.; Butkutė, S.; Žukauskas, A.; Vitta, P.; Kareiva, A. Sol-Gel Synthesized Far-Red Chromium-Doped Garnet Phosphors for Phosphor-Conversion Light-Emitting Diodes that Meet the Photomorphogenetic Needs of Plants. *Appl. Opt.* **2014**, *53*, 907–914.
- Kreslavski, V. D.; Fomina, I. R.; Los, D. A.; Carpenter, R.; Kuznetsov, V. V.; Allakhverdiev, S. I. Red and Near Infra-Red Signaling: Hypothesis and Perspectives. *J. Photochem. Photobiol., C* **2012**, *13*, 190–203.
- Karu, T. I.; Kolyakov, S. F. Exact Action Spectra for Cellular Responses Relevant to Phototherapy. *Photomed. Laser Surg.* **2005**, *23*, 355–361.
- Sontea, V.; Pocaznoi, I.; Furtuna, D.; Seryakov, A.; Barun, V.; Dick, S. Effects of The Low-Level Light Therapy on Skin Wound Using LED. IEEE E-Health and Bioengineering Conference, 2013; pp 1–4.
- Whelan, H. T.; Smits, R. L.; Buchman, E. V.; Whelan, N. T.; Turner, S. G.; Margolis, D. A.; Cevenini, V.; Stinson, H.; Ignatius, R.; Martin, T.; Cwiklinski, J.; Philipp, A. F.; Graf, W. R.; Hodgson, B.; Gould, L.; Kane, M.; Chen, G.; Caviness, J. Effect of NASA Light-Emitting Diode Irradiation on Wound Healing. *J. Clin. Laser Med. Surg.* **2001**, *19*, 305–314.
- Eells, J. T.; Henry, M. M.; Summerfelt, P.; Wong-Riley, M. T. T.; Buchmann, E. V.; Kane, M.; Whelan, N. T.; Whelan, H. T. Therapeutic Photobiomodulation for Methanol-Induced Retinal Toxicity. *Proc. Natl. Acad. Sci. U. S. A.* **2003**, *100*, 3439–3444.
- Ye, S.; Xiao, F.; Pan, Y. X.; Ma, Y. Y.; Zhang, Q. Y. Phosphors in Phosphor-Converted White Light-Emitting Diodes: Recent Advances in Materials, Techniques and Properties. *Mater. Sci. Eng., R* **2010**, *71*, 1–34.
- Chen, J. Y.; Zhang, N. M.; Guo, C. F.; Pan, F. J.; Zhou, X. J.; Suo, H.; Zhao, X. Q.; Goldys, E. M. Site-Dependent Luminescence and Thermal Stability of Eu^{2+} Doped Fluorophosphates toward White LEDs for Plant Growth. *ACS Appl. Mater. Interfaces* **2016**, *8*, 20856–20864.
- Li, J. H.; Yan, J.; Wen, D. W.; Khan, W. U.; Shi, J. X.; Wu, M. M.; Su, Q.; Tanner, P. A. Advanced Red Phosphors for White Light-Emitting Diodes. *J. Mater. Chem. C* **2016**, *4*, 8611–8623.
- van der Ende, B. M.; Aarts, L.; Meijerink, A. Lanthanide Ions as Spectral Converters for Solar Cells. *Phys. Chem. Chem. Phys.* **2009**, *11*, 11081–11095.
- Van de Haar, M. A.; Werner, J.; Kratz, N.; Hilgerink, T.; Tachikirt, M.; Honold, J.; Krames, M. R. Increasing The Effective Absorption of Eu^{3+} -Doped Luminescent Materials towards Practical Light Emitting Diodes for Illumination Applications. *Appl. Phys. Lett.* **2018**, *112*, 132101.
- McAuslan, D. L.; Longdell, J. J.; Sellars, M. J. Strong-Coupling Cavity QED Using Rare-Earth-Metal-Ion Dopants in Monolithic Resonators: What You Can Do with A Weak Oscillator. *Phys. Rev. A: At., Mol., Opt. Phys.* **2009**, *80*, 162307.
- Piao, X. Q.; Machida, K. I.; Horikawa, T.; Hanzawa, H.; Shimomura, Y.; Kijima, N. Preparation of $\text{CaAlSiN}_3:\text{Eu}^{2+}$ Phosphors by The Self-Propagating High-Temperature Synthesis and Their Luminescent Properties. *Chem. Mater.* **2007**, *19*, 4592–4599.
- Qin, X.; Liu, X. W.; Huang, W.; Bettinelli, M.; Liu, X. G. Lanthanide-Activated Phosphors Based on 4f-5d Optical Transitions: Theoretical and Experimental Aspects. *Chem. Rev.* **2017**, *117*, 4488–4527.
- Fang, Y.; Sojda, C. A.; Dey, G.; Teat, S. J.; Li, M.; Cotlet, M.; Zhu, K.; Liu, W.; Wang, L.; O'Carroll, D. M.; Li, J. Highly Efficient and Stable Blue-Excitable Yellow Phosphors Built on Multiple-Stranded One-Dimensional Inorganic-Organic Hybrid Chains. *Chem. Sci.* **2019**, *10*, 5363–5372.
- Fang, Y.; Liu, W.; Teat, S. J.; Dey, G.; Shen, Z. Q.; An, L. T.; Yu, D. C.; Wang, L.; O'Carroll, D. M.; Li, J. A Systematic Approach to Achieving High Performance Hybrid Lighting Phosphors with Excellent Thermal- and Photostability. *Adv. Funct. Mater.* **2017**, *27*, 1603444.
- Zhu, H. M.; Lin, C. C.; Luo, W. Q.; Shu, S. T.; Liu, Z. G.; Liu, Y. R.; Kong, J. T.; Ma, E.; Cao, Y. G.; Liu, R. S.; Chen, X. Y. Highly Efficient Non-Rare-Earth Red Emitting Phosphor for Warm White Light-Emitting Diodes. *Nat. Commun.* **2014**, *5*, 4312.
- GE Highlights Next Generation PFS/KSF Technologies at Display Week 2019. Website: <https://www.genewsroom.com/press-releases/ge-highlights-next-generation-pfsksf-technologies-display-week-2019>.
- Murphy, J. GE RadianRed Technology: Market Leading Wide Color Gamut Phosphor & Path Towards Enabling Next Generation Displays; SID/DSSC Business Conference, Display Week 2019, San Jose.
- Maiman, T. H. Stimulated Optical Radiation in Ruby. *Nature* **1960**, *187*, 493–494.
- Nie, Z. G.; Lim, K. S.; Zhang, J. H.; Wang, X. J. $\text{Pr}^{3+}\text{S}_0 \rightarrow \text{Cr}^{3+}$ Energy Transfer and ESR Investigation in Pr^{3+} ad Cr^{3+} Activated $\text{SrAl}_{12}\text{O}_{19}$ quantum cutting phosphor. *J. Lumin.* **2009**, *129*, 844–849.
- Könz, F.; Sun, Y.; Thiel, C. W.; Cone, R. L.; Equall, R. W.; Hutcheson, R. L.; Macfarlane, R. M. Temperature and Concentration Dependence of Optical Dephasing Spectral-Hole Lifetime, and Anisotropic Absorption in Eu^{3+} : Y_2SiO_5 . *Phys. Rev. B: Condens. Matter Mater. Phys.* **2003**, *68*, 085409.

- (25) Bindu, H. S.; Rao, T. R.; Raju, C. L. Spectroscopic and Radiative Properties of Sm³⁺ Ions in Zinc Borophosphate Glasses. *Phys. Scr.* **2015**, *90*, 065802.
- (26) Sokolska, I.; Kück, S. Optical Characterization of Cr³⁺ Doped LiTaO₃ Crystals Relevant for Laser Application. *Spectrochim. Acta, Part A* **1998**, *54*, 1695–1700.
- (27) Yu, D. C.; Rabouw, F. T.; Boon, W. Q.; Kieboom, T.; Ye, S.; Zhang, Q. Y.; Meijerink, A. Insights into The Energy Transfer Mechanism in Ce³⁺-Yb³⁺ Codoped YAG Phosphors. *Phys. Rev. B: Condens. Matter Mater. Phys.* **2014**, *90*, 165126.
- (28) Zhang, Z. Y.; Grattan, K. T. V.; Palmer, A. W. Temperature Dependence of Fluorescence Lifetime in Cr³⁺-Doped Insulating Crystals. *Phys. Rev. B: Condens. Matter Mater. Phys.* **1993**, *48*, 7772–7778.
- (29) Yamaga, M.; Macfarlane, P. I.; Henderson, B.; Holliday, K.; Takeuchi, H.; Yosida, T.; Fukui, M. Substitutional Disorder and The Ground State Spectroscopy of Gallogermanate Crystals. *J. Phys.: Condens. Matter* **1997**, *9*, 569–578.
- (30) Blasse, G.; Grabmaier, B. C. *Luminescent Materials*; Springer-Verlag: Berlin, 1994.
- (31) Shannon, R. D. Revised Effective Ionic Radii and Systematic Studies of Interatomic Distances in Halides and Chalcogenides. *Acta Crystallogr., Sect. A: Cryst. Phys., Diff., Theor. Gen. Crystallogr.* **1976**, *32*, 751–767.
- (32) Yeh, C. W.; Chen, W. T.; Liu, R. S.; Hu, S. F.; Sheu, H. S.; Chen, J. M.; Hintzen, H. T. Origin of Thermal Degradation of Sr_{2-x}Si_xN₈: Eu_x Phosphors in Air for Light-Emitting Diodes. *J. Am. Chem. Soc.* **2012**, *134*, 14108–14117.
- (33) Spearing, D. R.; Stebbins, J. F.; Farnan, I. Diffusion and The Dynamics of Displacive Phase Transitions in Cryolite (Na₃AlF₆) and Chiolite (Na₂Al₂F₁₄): Multi-Nuclear NMR Studies. *Phys. Chem. Miner.* **1994**, *21*, 373–386.
- (34) Wei, L. L.; Lin, C. C.; Wang, Y. Y.; Fang, M. H.; Jiao, H.; Liu, R. S. Photoluminescent Evolution Induced by Structural Transformation Through Thermal Treating in The Red Narrow-Band Phosphor K₂GeF₆: Mn⁴⁺. *ACS Appl. Mater. Interfaces* **2015**, *7*, 10656.
- (35) Payne, S. A.; Chase, L. L.; Smith, L. K.; Kway, W. L.; Newkirk, H. W. Laser Performance of LiSrAlF₆: Cr³⁺. *J. Appl. Phys.* **1989**, *66*, 1051–1506.
- (36) Liu, C. Y.; Xia, Z. G.; Chen, M. Y.; Molokeev, M. S.; Liu, Q. L. Near-Infrared Luminescence and Color Tunable Chromophores Based on Cr³⁺-Doped Mullite-Type Bi₂(Ga,Al)₄O₉ Solid Solutions. *Inorg. Chem.* **2015**, *54*, 1876–1882.
- (37) Chen, D. Q.; Wan, Z. Y.; Zhou, Y.; Zhou, X. Z.; Yu, Y. L.; Zhong, J. S.; Ding, M. Y.; Ji, Z. G. Dual-Phase Glass Ceramic: Structure, Dual-Modal Luminescence, and Temperature Sensing Behaviors. *ACS Appl. Mater. Interfaces* **2015**, *7*, 19484–19493.
- (38) Malysa, B.; Meijerink, A.; Jüstel, T. Temperature Dependent Cr³⁺ Photoluminescence in Garnets of The Type X₃Sc₂Ga₃O₁₂ (X = Lu, Y, Gd, La). *J. Lumin.* **2018**, *202*, 523–531.
- (39) Yu, D. C.; Marín-Rodíguez, R.; Zhang, Q. Y.; Meijerink, A.; Rabouw, F. T. Multi-Photon Quantum Cutting in Gd₂O₂S: Tm³⁺ to Enhance The Photo-Response of Solar Cells. *Light: Sci. Appl.* **2015**, *4*, e344.
- (40) Torchia, G. A.; Schinca, D.; Khaidukov, N. M.; Tocho, J. O. The Luminescent Quantum Efficiency of Cr³⁺ Ions in Cs₂NaAlF₆ Single Crystals. *Opt. Mater.* **2002**, *20*, 301–304.
- (41) Wei, Y.; Qi, X. H.; Xiao, H.; Luo, W. Z.; Yao, H.; Lv, L. F.; Li, G. G.; Lin, J. Site-Preferential Occupancy Induced Photoluminescence Tuning in (Ca,Ba)₅(PO₄)₃Cl:Eu²⁺ Phosphors. *RSC Adv.* **2016**, *6*, 43771–43779.
- (42) Dorenbos, P. A Review on How Lanthanide Impurity Levels Change With Chemistry and Structure of Inorganic Compounds. *ECS J. Solid State Sci. Technol.* **2013**, *2*, R3001–R3011.
- (43) Pust, P.; Weiler, V.; Hecht, C.; Tücks, A.; Wochnik, A. S.; Henß, A.-K.; Wiechert, D.; Scheu, C.; Schmidt, P. J.; Schnick, W. Narrow-Band Red-Emitting Sr[LiAl₃N₄]: Eu²⁺ as A Next-Generation LED-Phosphor Material. *Nat. Mater.* **2014**, *13*, 891–896.
- (44) Kim, Y. H.; Arunkumar, P.; Kim, B. Y.; Unithrattil, S.; Kim, E.; Moon, S.-H.; Hyun, J. Y.; Kim, K. H.; Lee, D.; Lee, J.-S.; Im, W. B. A Zero-Thermal-Quenching Phosphor. *Nat. Mater.* **2017**, *16*, 543–550.
- (45) #960000 Color Hex. Website: <http://www.color-hex.com/color/960000>.